

Comparison of Evaporation and Cold Pool Development between Single-Moment and Multimoment Bulk Microphysics Schemes in Idealized Simulations of Tornadic Thunderstorms

DANIEL T. DAWSON II AND MING XUE

Center for Analysis and Prediction of Storms, and School of Meteorology, University of Oklahoma, Norman, Oklahoma

JASON A. MILBRANDT

Meteorological Research Division, Environment Canada, Dorval, Québec, Canada

M. K. YAU

McGill University, Montreal, Quebec, Canada

(Manuscript received 26 January 2009, in final form 1 October 2009)

ABSTRACT

Idealized simulations of the 3 May 1999 Oklahoma tornadic supercell storms are conducted at various horizontal grid spacings ranging from 1 km to 250 m, using a sounding extracted from a prior 3-km grid spacing real-data simulation. A sophisticated multimoment bulk microphysics parameterization scheme capable of predicting up to three moments of the particle or drop size distribution (DSD) for several liquid and ice hydrometeor species is evaluated and compared with traditional single-moment schemes. The emphasis is placed on the impact of microphysics, specifically rain evaporation and size sorting, on cold pool strength and structure, and on the overall reflectivity structure of the simulated storms. It is shown through microphysics budget analyses and examination of specific processes within the low-level downdraft regions that the multimoment scheme has important advantages, which lead to a weaker and smaller cold pool and better reflectivity structure, particularly in the forward-flank region of the simulated supercells. Specifically, the improved treatment of evaporation and size sorting, and their effects on the predicted rain DSDs by the multimoment scheme helps to control the cold bias often found in the simulations using typical single-moment schemes. The multimoment results are more consistent with observed (from both fixed and mobile mesonet platforms) thermodynamic conditions within the cold pools of the discrete supercells of the 3 May 1999 outbreak.

1. Introduction

A long-standing challenge in numerical simulation and prediction of 3D deep moist convection is the parameterization of cloud and precipitation microphysics. Most numerical studies of 3D deep moist convection have relied on bulk microphysics parameterizations (BMP, or simply “scheme”), in which a certain functional form for the particle or drop size distribution (DSD) of one or more categories of cloud and hydrometeor species is prescribed. Based on observational

studies, particularly Marshall and Palmer (1948) and Gunn and Marshall (1958), an exponential distribution is often used, with the following form:

$$N_x(D) = N_{0x} \exp(-\lambda_x D), \quad (1)$$

where $N_x(D)$ is the number density as a function of particle diameter D , N_{0x} is the intercept parameter, and λ_x is the slope parameter, and the subscript x is a placeholder for a given species (hereafter we will omit the x subscript for clarity). Although (1) has two free parameters, they are not independent in most applications. Typically, one of the parameters (usually N_0) is fixed or diagnosed as a single-value function of the other, and the hydrometeor mixing ratio is predicted, which is proportional to $M(3)$, the third moment of the DSD. This

Corresponding author address: Daniel T. Dawson II, NOAA/National Severe Storms Laboratory, National Weather Center, 120 David L. Boren Blvd., Norman, OK 73072.
E-mail: Dan.Dawson@noaa.gov

quantity can then be used, along with the fixed (or diagnosed) parameter, to determine the value of the remaining free parameter, thus closing the system. Such BMPs are known as single-moment (SM) schemes because only one moment of the DSD is predicted.

Equation (1) is a special case of the gamma distribution function, often written as

$$N(D) = N_0 D^\alpha e^{-\lambda D}, \quad (2)$$

where α is the shape parameter. Note that (2) reduces to (1) for $\alpha = 0$. The p th moment of this DSD is given by

$$M(p) = \frac{N_0}{\lambda^p} \frac{\Gamma(1 + \alpha + p)}{\Gamma(1 + \alpha)}. \quad (3)$$

Ulbrich (1983) suggested that the gamma function better characterizes many observed raindrop size distributions, and allows more flexibility in describing the relative number concentrations of large versus small drops. The distribution has also been applied to other types of hydrometeors, including cloud and various ice categories (Walko et al. 1995; Meyers et al. 1997; Milbrandt and Yau 2005a, hereafter MY05a; Milbrandt and Yau 2005b, hereafter MY05b). By adopting (2) and by predicting more than one moment of the size distribution, it is possible to develop multimoment (MM) schemes that allow α , N_0 , and λ to vary independently (MY05a,b).

The MM schemes have a number of advantages over SM schemes. Several researchers (e.g., MY05a,b; Ferrier 1994; Ferrier et al. 1995; Straka et al. 2005; Seifert 2008) have pointed out that in processes like accretion, diffusion, evaporation, and sedimentation, the number concentration and mixing ratio can vary independently so the assumption of constant N_0 in a SM scheme is invalid. During sedimentation, the size distribution can become narrower from size sorting (MY05a), which is not permitted in SM schemes because a single fall speed for the predicted moment for a hydrometeor category is used. On the other hand, MM schemes allow for a size-sorting mechanism through differential sedimentation of the predicted moments. MY05a showed that a triple-moment (TM) BMP was able to closely reproduce the effect of size sorting on the size distribution of precipitating hydrometeors as simulated by an analytical bin model (see their Fig. 3). Of course no bulk schemes actually treat size sorting explicitly; they can at best allow for a mechanism to mimic its effect on the distribution. To elaborate, in a DM scheme, for example, the number-weighted fall speed V_N is always less than the mass-weighted fall speed V_Q , leading to an overall tendency for a given magnitude of q to be associated with smaller N as one moves down in the atmosphere, which is physically equivalent to larger particles falling faster than smaller ones.

We will return to this point later, but the reader is referred to MY05a for a further detailed description of this process. For completeness, we point out that some BMPs try to emulate a bin model for specific processes through the use of lookup tables (Saleeby and Cotton 2004). This approach attempts to reduce the error inherent in using a single bulk value (as in most BMPs) for such parameters as collection efficiency or fall speed, although the form of the distribution is still specified, unlike in a full bin scheme.

Recently, MM schemes have enjoyed increasing popularity in cloud and storm modeling (Ferrier et al. 1995; Meyers et al. 1997; Reisner et al. 1998; Seifert and Beheng 2001; Seifert and Beheng 2006; Seifert et al. 2006; Mansell 2008; Morrison et al. 2009). Ferrier et al. (1995) and Morrison et al. (2009), examined the impact of a double-moment (DM) scheme on simulations of idealized 2D squall lines. They found that the stratiform region typically has a smaller N_0 than the convective region and therefore the DM scheme performed much better than the fixed- N_0 SM scheme. Mansell (2008) compared DM and SM schemes for ensemble Kalman filter (EnKF) experiments for a tornadic supercell storm and noted a better representation of the cold pool structure and forward-flank reflectivity region of the supercell when using the DM scheme. The results of these studies suggest that allowing more parameters of the various hydrometeor DSDs to vary independently in time and space, as in MM schemes, improves the overall simulation of convective storms, with much less case-specific “tuning” of the parameters necessary.

A primary motivation for this study comes from the experience that many past numerical simulations of supercell convection produce cold pools that are too large and intense. Markowski et al. (2002) attributed this bias at least partially to the use of warm-rain-only instead of ice microphysics. Gilmore and Wicker (1998) found through numerical simulations that large and strong cold pools were produced as a result of midlevel dry air reaching the surface in the downdrafts, and that the drier the air, the stronger the cold pools tended to be, because of enhanced evaporation potential. They used a warm-rain scheme and did not otherwise investigate the impact of microphysics. This result, however, has been recently brought into question by James and Markowski (2010), who found that ice microphysics (both SM and DM) generally resulted in stronger (weaker) cold pools for a moist (dry) sounding, in contrast to Gilmore and Wicker (1998). They also suggested that the results of Gilmore and Wicker (1998) and other similar idealized studies were due to their choice of a warm-rain-only scheme. As will be seen in this paper, however, a cold bias still appears to exist with SM schemes even with ice

when typical values of the intercept parameter for rain and hail are used.

In addition to the well-known cold bias, several studies with SM BMPs have shown that simulated storm properties, including precipitation intensity and amount, propagation speed and direction, general storm morphology, and cold pool size and intensity, are very sensitive to the choice of N_0 for rain and hail, or alternatively the choice of characteristic diameter D_n (Gilmore et al. 2004; van den Heever and Cotton 2004; Snook and Xue 2008). However, observational studies have shown that N_0 varies considerably in time and space for convection (e.g., Waldvogel 1974), which suggests that more sophisticated MM schemes may be more appropriate for simulations. Understanding the impact of DSD variations in the rain category on the low-level downdrafts and cold pools of simulated severe (specifically supercell) convection, which can then be generalized to other hydrometeor categories, is the main goal of this study. In this paper, we report on high-resolution (1-km or smaller horizontal grid spacing) idealized simulations of supercell storms in the 3 May 1999 Oklahoma tornado outbreak, with an emphasis on comparing results using MM BMPs with those using SM BMPs with different values of the rain intercept parameter. We also qualitatively compare the simulations with available surface observations (both mobile and fixed) on cold pool size and intensity. Future papers will address more realistic real-data simulations using MM microphysics of this outbreak, and a more rigorous comparison with observations.

We will focus on the rain category in this paper, mainly for the sake of brevity and since the arguments herein regarding the benefits of MM over SM also apply qualitatively to the hail category. It is known that variations in the hail category have a strong impact on storm simulations (Gilmore et al. 2004; van den Heever and Cotton 2004). Furthermore, since these and other studies have examined the sensitivity of simulated supercell storms to parameters in a SM scheme, we will instead focus on the results obtained with the MM schemes and the advantages and disadvantages over using the more common SM approach. Specifically, we show that certain important advantages of MM schemes over their SM counterparts with regard to their treatment of evaporation and size-sorting effects on the predicted DSDs of rain help to control the cold bias seen in many simulated convective storm downdrafts and associated cold pools. This long-standing problem is thus shown to be primarily a microphysics parameterization issue, and the results have broad implications for storm-scale numerical weather prediction (NWP) and simulation. A budget analysis of the thermodynamically active microphysical processes (primarily melting/freezing, evaporation/condensation,

and collection between liquid and ice categories) within the low-level downdrafts will be performed.

Two BMP schemes are examined. One is the popular Lin et al. (1983) ice BMP, as modified by Tao and Simpson (1993). This scheme, hereafter referred to as LIN, is the default ice BMP in the Advanced Regional Prediction System (ARPS; Xue et al. 2000, 2003), the model used in this investigation. The LIN scheme is a SM three-class ice scheme that predicts the mixing ratios of cloud water, rainwater, ice crystals, snow aggregates, and graupel/hail, while holding the intercept parameter for each precipitating species—rain, snow, and graupel/hail—fixed. The cloud and ice species are assumed to have negligible terminal velocities and are described as monodispersed. The other is the MM scheme of Milbrandt and Yau (MY05a,b; Milbrandt and Yau 2006a, hereafter MY06a; Milbrandt and Yau 2006b, hereafter MY06b). This scheme, recently incorporated into the ARPS model and hereafter referred to as MY, predicts up to three moments of the DSD for each of the five classes of precipitating hydrometeors (rain, ice crystals, snow, graupel, and hail). Cloud water is assumed to have negligible terminal velocity with its DSD described by a gamma distribution with two specified shape parameters (MY05b). In contrast to the LIN scheme, which treats only hail (although graupel-like behavior can be simulated with appropriate choice of the intercept parameter and bulk density, as in Gilmore et al. 2004), the MY scheme contains separate categories for graupel and hail. The three predicted moments in MY are $M(0)$, $M(3)$, and $M(6)$, proportional to the total number concentration N , the mixing ratio q , and the radar reflectivity factor Z , respectively. With the full TM formulation, all three parameters in (2) vary independently, while for the DM and SM versions, one or both of these parameters must be fixed or diagnosed. With reference to the MY scheme, we will adopt the abbreviations MY1, MY2, MY2DA, and MY3 to signify the number of moments predicted (see Table 1 for a description). Here MY2DA refers to the diagnostic- α scheme, as described in MY05a,b.

This paper is organized as follows. In section 2, we provide a brief overview of the 3 May 1999 tornado outbreak. In section 3, the design of the idealized supercell simulation experiments is described. Section 4 describes the results, including a budget analysis, and provides physical explanations for the differences between the BMPs. As previously stated, the main goal of this study is to examine the impact of the variations of rain DSDs on the low-level downdraft and cold pool development, and a detailed discussion of the results in this context is provided. Section 5 summarizes the paper and discusses ongoing and future work.

TABLE 1. List of microphysics schemes and their descriptions.

Microphysics scheme/configuration	Description
LINA	Based on Lin et al. (1983) and Tao and Simpson (1993)
LINB	LIN scheme with N_{0r} reduced from default value of $8.0 \times 10^6 \text{ m}^{-4}$ to $4.0 \times 10^5 \text{ m}^{-4}$
MY1	Single-moment version of the MY scheme (q predicted)
MY2	Double-moment version of the MY scheme (q and N_t predicted)
MY2DA	As in MY2 but with diagnostic relations for shape parameter α
MY3	Triple-moment version of the MY scheme (q , N_t , and Z predicted)

2. Overview of the 3 May 1999 Oklahoma tornado outbreak

The 3 May 1999 tornado outbreak was characterized by several long-track, and in some cases violently tornadic supercells that tracked across central Oklahoma. The storms were noteworthy for producing over 70 tornadoes in Oklahoma alone, including the deadly F5 tornado that struck parts of Moore and southern Oklahoma City, Oklahoma. Available data, such as observations from Markowski (2002), and Oklahoma Mesonet observations, suggested mostly localized and relatively weak cold pools (i.e., maximum equivalent potential temperature deficits on the order of 5 K or less) associated with the discrete supercells, at least during the

first several hours of the event. Roebber et al. (2002) and Thompson and Edwards (2000) provide an overview of the synoptic weather conditions associated with this outbreak. Figure 1 shows an objective analysis of surface equivalent potential temperature θ_e at 0000 UTC 4 May 1999, during the early stages of the outbreak. Two of the tornadic supercells of the outbreak, labeled A and B after Speheger et al. (2002), are indicated. Storm A produced a large F5-intensity tornado at the time of this analysis. Even though the still insufficient observation density of the Oklahoma Mesonet (~ 30 km spacing) precludes detailed analyses of storm cold pools, it can be seen nevertheless that strong and extensive cold pools associated with the discrete supercells are absent in the analysis. Markowski (2002) reports on mobile mesonet observations of the storms of this day, and indicates that the rear-flank downdrafts (RFDs) were relatively warm and buoyant (θ_e deficits on the order of a few degrees kelvin) and it may have helped tornadogenesis. The subject of tornadogenesis is beyond the scope of this paper but will be pursued in future papers.

3. Experiment design

a. Sounding used for idealized experiments

Dawson et al. (2007) has performed a real data simulation of this case at a grid spacing of 3 km. They found that cold pool strength and size were consistently overpredicted for each of the BMPs examined. It was speculated that the relatively coarse grid resolution—on

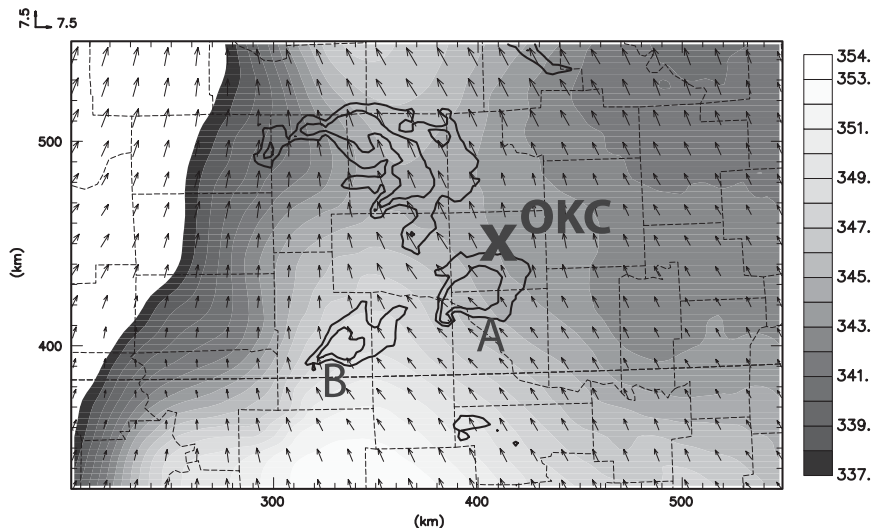


FIG. 1. Objective analyses of surface θ_e (grayscale), observed reflectivity (black contours, 20-dBZ increment) and horizontal wind vectors (every 15 km, scale in m s^{-1} indicated in lower left of figure) that include Oklahoma Mesonet data, at 0000 UTC 4 May 1999 centered over central Oklahoma. Oklahoma City is labeled OKC.

which turbulent mixing processes, which would act to dilute the downdrafts, are poorly represented—was a possible reason for the overly intense cold pools and may have affected microphysical processes such as rain evaporation. To examine the impact of microphysics in more detail at higher grid resolutions, we focus in this paper on a systematic set of idealized simulations that use a single sounding to define the environment and do not include radiation or surface physics processes. While the absence of surface friction may affect the cold pool propagation somewhat, its inclusion tends to modify the environmental wind profile over time, which is undesirable for the purposes of these simulations, and thus the role of surface fluxes in facilitating recovery of the cold pool is not taken into account. However, preliminary results from real-data simulations of this outbreak, in a manuscript being prepared for publication, indicate that, at least in this case, the differences in microphysics appear to overwhelm any mitigating effect from the surface fluxes, at least on time scales on the order of a few hours.

The sounding used for the idealized experiments was extracted from the 1-h forecast (valid at 2300 UTC) of the 3-km LIN simulation of Dawson et al. (2007) at a location that was determined in reference to the Oklahoma surface Mesonet observations to be more representative of the unstable inflow region of the storms during the early stages of their tornado-producing phase. The observed Norman, Oklahoma (OUN), sounding at 0000 UTC 4 May 1999 is believed to represent more of the environment after the storms reached maturity.

This extracted sounding has a similar wind profile to the observed OUN sounding, but the temperature and moisture profiles are significantly different (see Fig. 2). Figure 3 shows the vertical profile of θ_e for the OUN and extracted soundings. The vertical gradient in θ_e above the boundary layer is similar in both soundings, as is the minimum value, but the height of the minimum θ_e is higher in the extracted sounding. Moreover, the θ_e values in the boundary layer are larger in the extracted sounding, due to the higher temperatures and moisture content as opposed to the observed sounding. The large CAPE difference between the two soundings is due to the cooler surface temperatures in the observed sounding as well as the fact that the observed sounding was truncated in the upper levels, preventing a full CAPE calculation. With the strong cap and the absence of any mesoscale or synoptic-scale forcing in the idealized simulations, the observed sounding was found to be unable to sustain storms in the model. This is another reason that we chose to use the extracted sounding. Finally, we point out that the environmental sounding can have a significant impact on cold pool strength (see, e.g.,

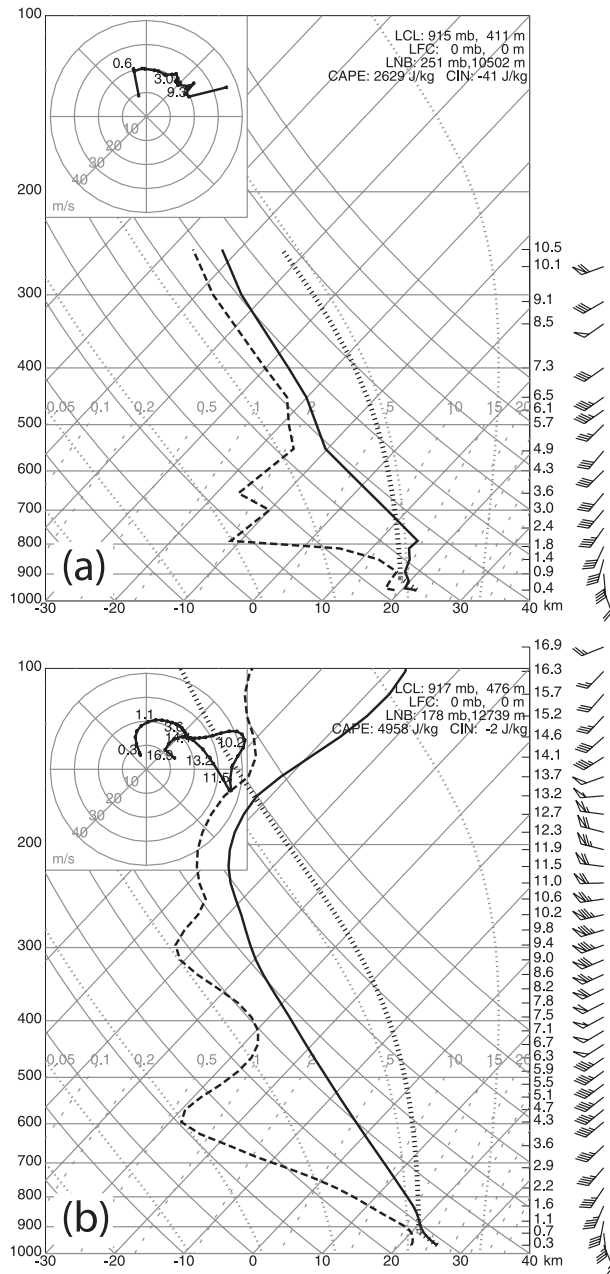


FIG. 2. (a) Observed OUN sounding at 0000 UTC 4 May 1999 and (b) model extracted sounding at 2300 UTC (1-h forecast) from the 3-km LINA experiment of Dawson et al. (2007) in the inflow region of the simulated supercell storms.

Gilmore and Wicker 1998; McCaul and Cohen 2002; James and Markowski 2010). A broader investigation of the role of the environmental sounding in modulating the impact of BMPs is planned in future work, but is beyond the scope of the current study, which is concerned with the differences in BMPs for a single environment.

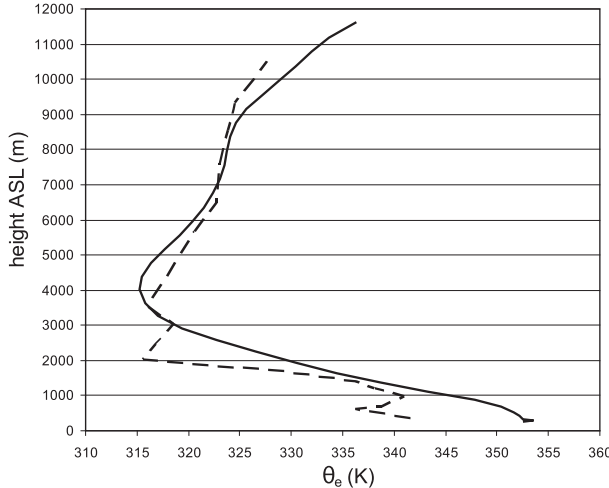


FIG. 3. Vertical profile of θ_e for the extracted (solid) and observed 0000 UTC Norman (OUN, dashed) soundings.

b. Idealized experiments

Idealized experiments allow us to focus on the effects of the BMPs and allow for a large set of experiments at high resolutions before retuning to more realistic settings. Bryan et al. (2003) suggests that grid spacings much smaller than 1 km may be necessary to properly resolve convection. We conduct a series of simulations at 1-km, 500-m, and 250-m horizontal grid spacings, which included the simple monotonic fourth-order computational mixing scheme of Xue (2000) whose coefficients are 0.0005, 0.0015, and 0.002 s^{-1} , respectively, for the three grid spacings. Fifty-three vertical levels were used, with a grid spacing of 20 m at the surface, stretched to 800 m at the model top (approximately 20 km). This vertical grid setup yields 6 vertical levels in the lowest 1 km AGL, and 10 in the lowest 2 km.

We tested a total of six schemes or their variations. They include two variations of the Lin scheme where N_{0r} was set to the typical Marshall and Palmer (1948) value of $8.0 \times 10^6 \text{ m}^{-4}$ (LINA) or to a reduced value of $4.0 \times 10^5 \text{ m}^{-4}$ (LINB). The other four forecasts used the SM, DM, the DM scheme with diagnostic α (MY2DA) and TM versions of MY scheme, respectively (Table 1). All simulations are otherwise identical. The experiment naming convention throughout the paper will follow the template $[\Delta x]/[scheme]$, where $[\Delta x]$ denotes the horizontal grid spacing and $[scheme]$ denotes the BMP configuration as given in Table 1. For example, experiment 500mMY2 has a 500-m grid spacing and uses the MY2 scheme. Table 2 indicates the values of the intercept parameter for each of the precipitating categories for each of the SM schemes, where applicable.

For both the 1-km and 500-m simulations, a grid of $128 \times 175 \times 20 \text{ km}^3$ was used. Convection was initiated with

TABLE 2. Intercept parameter values for precipitating categories used in the experiments with single-moment microphysics schemes. Here, MD stands for a monodisperse distribution and $f(T)$ refers to the temperature-dependent N_0 used for cloud ice (see MY05b).

Scheme	LINA	LINB	MY1
$N_{0r} (\times 10^6 \text{ m}^{-4})$	8.0	0.4	8.0
$N_{0i} (\times 10^6 \text{ m}^{-4})$	MD	MD	$f(T)$
$N_{0s} (\times 10^6 \text{ m}^{-4})$	3.0	3.0	3.0
$N_{0g} (\times 10^6 \text{ m}^{-4})$	NA	NA	0.4
$N_{0h} (\times 10^6 \text{ m}^{-4})$	0.04	0.04	0.04

an ellipsoidal thermal bubble of maximum potential temperature perturbation of 4 K with a horizontal radius of 10 km and vertical radius of 1.5 km, centered 1.5 km above ground, and 35 and 25 km from the west and south edge of the domain, respectively. The simulations were run out to 2 h. Two additional sets of experiments with thermal bubbles of maximum potential temperature perturbations of 8 and 2 K, respectively, were also performed. In the 8-K case, the storms developed more rapidly but also decayed quickly (by approximately 1 h; that is, they were “pulse” storms). Otherwise the evolution of the cold pools was qualitatively similar to those of the 4-K case. In the 2-K case, no sustained deep convection formed in any of the simulations. For the 250-m simulations, a smaller $64 \times 64 \times 20 \text{ km}^3$ grid was used, and the initial thermal bubble has the same dimensions and location relative to the southern and western boundaries. In addition, for the 250-m simulations only, the environmental sounding was modified to remove the mean storm motion to keep the storm within the smaller domain. To verify that the use of a smaller domain with a storm-relative sounding did not significantly impact the results, we also repeated the 500-m simulations using the 250-m configuration described above. The results were not significantly different than on the original $128 \times 175 \times 20 \text{ km}^3$ grid. Finally, the 250-m simulations were performed only for the MY suite of MP schemes.

4. Results and discussion

a. Cold pool and reflectivity structure

Even with the extracted forecast sounding, the storm in the 1-km experiments decayed in less than 1 h; a sustained storm could not be maintained. Within this initial period, 1kmLINA and 1kmMY1 exhibited more rapid cold pool development than in the other runs (not shown). At 500-m grid spacing, most experiments produced a storm that lasted through most of the 2-h simulation (Fig. 4). Time series of cold pool area, minimum θ'_e , and average θ'_e are shown in Fig. 5. The cold pool at

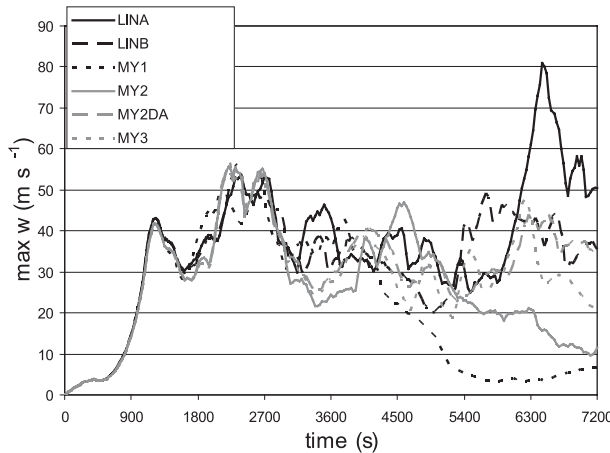


FIG. 4. Domain-maximum vertical velocity vs time for the 500-m simulations.

the surface is defined as that area enclosed by the $-1\text{-K } \theta'_e$ contour, where θ'_e is defined as departure from the domain-wide horizontal average of θ_e . In this study, we calculate θ_e according to Bolton (1980). We use θ_e to discriminate the cold pool because it takes into account both temperature and moisture effects, and also serves as a proxy for the source region of the cold pool air (i.e., lower magnitudes indicate descent from a higher altitude, assuming conservation of θ_e), though we stress that this can be interpreted in only a qualitative sense, since

θ_e is not actually conserved in downdrafts because of processes such as turbulent mixing and melting of ice. A trajectory analysis was performed to determine the source height of parcels reaching the surface at the minimum θ'_e in the cold pool for each simulation. The results (not shown) indicate that the stronger the cold pool, the higher the level the parcel originated; the SM runs all had maximum cold pool parcel source heights ranging from 2 to 3 km AGL, while the MM runs were clustered farther down, near 1 km AGL.

Referring to Fig. 5a, the cold pool first develops after about 1800 s in all simulations and increases steadily in size thereafter. The rate of increase of size, however, is much greater in 500mMY1 and 500mLINA, while the MM runs are all very similar to each other and 500mLINB. By the end of the 2-h simulation period, the cold pool in 500mMY1 is roughly 3.5 times the size of that in 500mMY2, 500mMY2DA, 500mMY3, and 500mLINB, and roughly 1.5 times the size of that in 500mLINA. Despite the fact that 500mLINB shows a similar cold pool size to the MM runs, it displays both colder minimum θ'_e and mean θ'_e (Figs. 5b,c), more similar to the other SM runs. This may be because, while the surface cold pool air in 500mLINB is overall potentially colder than in the MM runs, it shows similar temperature perturbations (approximately -2 to $+2$ K at most, not shown) to the MM runs. Since gust front speed propagation is, to a first-order approximation, a function

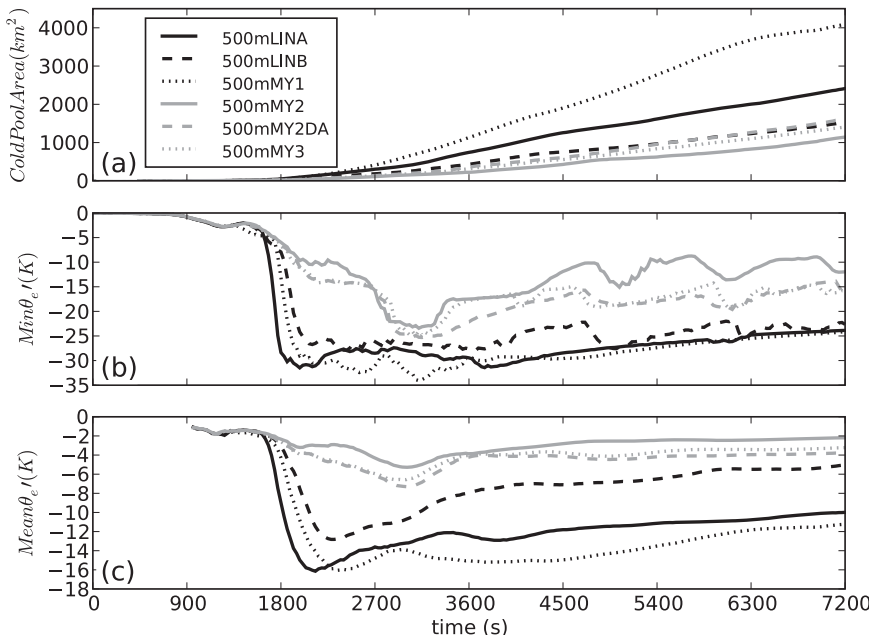


FIG. 5. Time series of (a) total surface cold pool area as defined as the sum of the area of all grid squares with $\theta'_e < -1\text{ K}$, (b) minimum θ'_e at the surface, and (c) mean θ'_e within the cold pool as defined above, for each of the 500-m experiments.

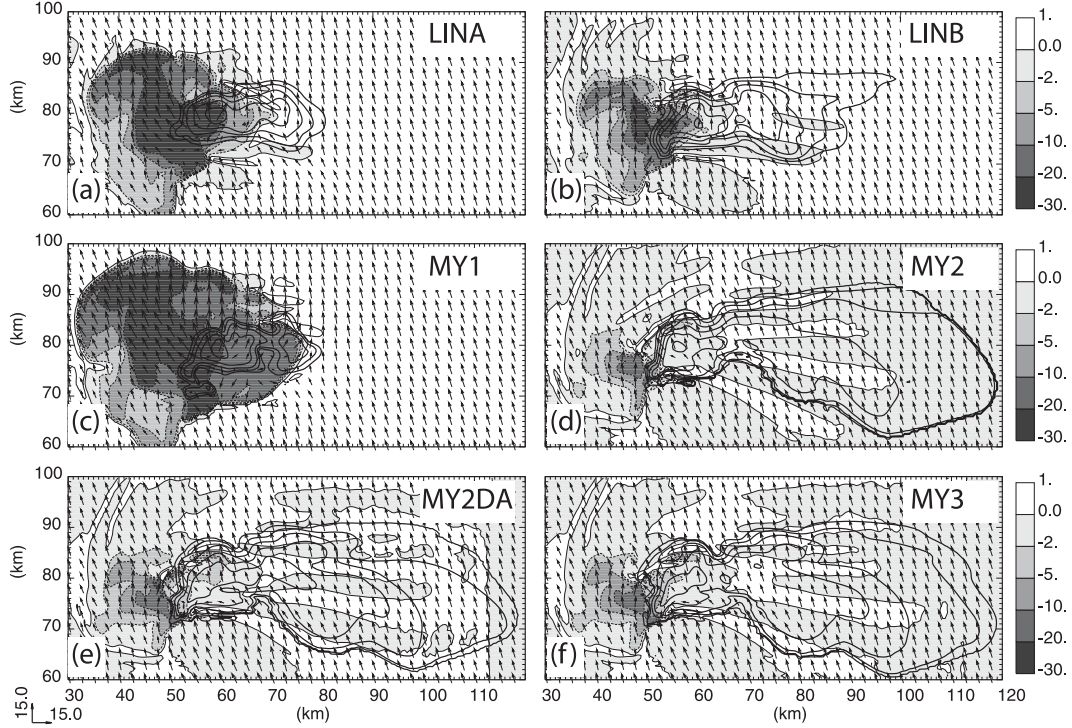


FIG. 6. Surface equivalent potential temperature perturbation (grayscale filled contours), reflectivity (heavy contours, 10-dBZ increment), and horizontal wind vectors (plotted every 2.5 km, 1 step = 15 m s^{-1}) for the 500-m simulations at 3600 s: (a) 500mLINA, (b) 500mLINB, (c) 500mMY1, (d) 500mMY2, (e) 500mMY2DA, and (f) 500mMY3. Vectors in this and all subsequent figures are ground relative.

of the temperature perturbation, this result makes physical sense. Also, despite the steady increase in cold pool size, the strength of the cold pool actually shows a slight overall weakening trend after about 3600 s in all simulations. The exact cause of this weakening trend is unknown, but may be related to the leveling off (and in some cases, weakening) of the storm intensity after 1 h of simulation (cf. Fig. 4).

Figure 6 shows snapshots of the θ'_e fields and simulated radar reflectivity at the surface for the various runs. The radar reflectivity is calculated for each run assuming Rayleigh scattering theory according to Eq. (7) of MY05a. Recall that Z is only predicted for the MY3 scheme, and N_t only for the MY2, MY2DA, and MY3 schemes. Thus, while Z is directly available to be converted to equivalent radar reflectivity in MY3, it must be first diagnosed from the other predicted moments and fixed/diagnosed DSD parameters for all the other schemes. All ice hydrometeors are assumed dry for the purposes of the radar reflectivity calculation. The cold pool structures in the DM and TM runs (Figs. 6d–f) are similar and are much smaller and weaker than those in the SM (Figs. 6a–c) cases (except for 500mLINB). The SM runs (500mLINA, 500mLINB, and 500mMY1) also vary significantly amongst themselves in terms of the

cold pool strength and size, with 500mLINB having the weakest (in terms of θ'_e) and smallest cold pool, consistent with the reduced N_{0r} value used. This result is also consistent with previous studies on the impact of varying N_{0r} , or N_{0h} (Gilmore et al. 2004; Snook and Xue 2008), or alternatively D_{nh} (van den Heever and Cotton 2004).

Interestingly, the supercell storms in the SM runs are generally characterized by a prominent cold pool in the forward-flank downdraft (FFD) region at the surface (cf. Figs. 6a–c), whereas the DM and TM schemes produce a much weaker or even nonexistent cold pool in that region (cf. Figs. 6d–f), a region where the FFD is defined in the classic supercell conceptual model (see, e.g., Lemon and Doswell 1979; Doswell and Burgess 1993). This latter result compares favorably with available surface mesonet observations in the forward flanks of the two most prominent supercells on 3 May 1999 (Fig. 7); the observations show temperature deficits of at most 2–3 K and dewpoint temperatures that actually increase slightly. This is consistent with the subsaturated boundary layer inflow air at the lower levels being driven toward its wet-bulb temperature by evaporation of falling rain. The MM simulations appear to reproduce these conditions in the forward flank, while the SM simulations in general

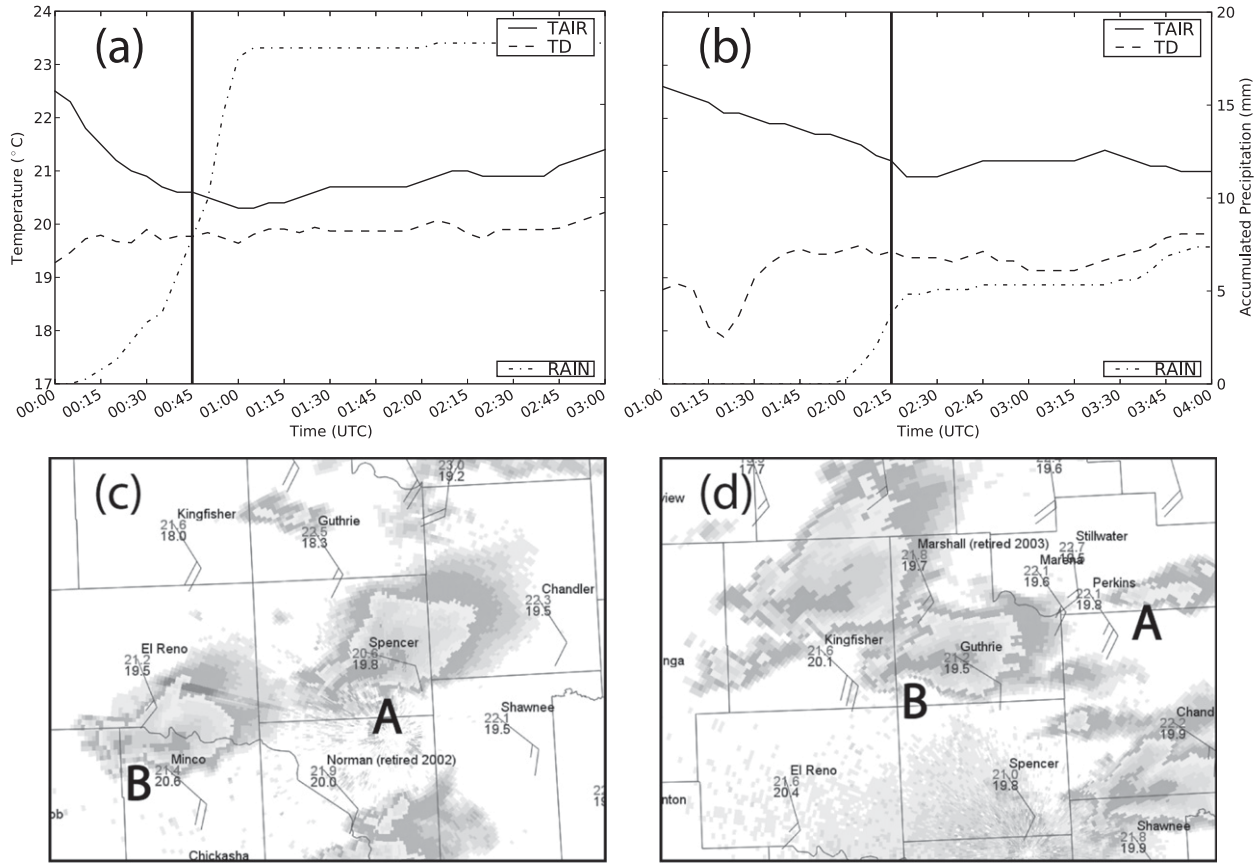


FIG. 7. (a) Time series from 1900 CDT 3 May 1999 (0000 UTC 4 May 1999) to 2200 CDT 3 May 1999 (0300 UTC 4 May 1999) for the Spencer mesonet station during the passage of the forward flank. Temperature and dewpoint traces ($^{\circ}\text{C}$) are solid and dashed lines, respectively, and the accumulated precipitation (mm) is a dot-dash line. The thick vertical black bar marks the time of the image in (c). (b) As in (a), but for the Guthrie mesonet station from 2000 CDT (0100 UTC) to 2300 CDT (0400 UTC). Corresponding base reflectivity (0.5° tilt) images from the KTLX radar and surrounding mesonet station observations (temperature in gray, dewpoint in black, and wind barbs, with full barb equal to 5 m s^{-1} , and half barb 2.5 m s^{-1}) are in (c) and (d). Also labeled in (c) and (d) are the main supercell storms A and B.

have temperature and dewpoint deficits consistent with drier, lower- θ_e air from higher levels reaching the surface in the downdrafts.

The reflectivity structure in the forward-flank region in the DM and TM simulations also compare much better to the observations in both shape and orientation, relative to the SM runs (cf. Figs. 7c,d with Fig. 6). In addition, the spatial east–west gradient of the reflectivity field in the forward flank is more realistic with the MY2DA and MY3 schemes than with MY2. We believe this to be related to the excessive hydrometeor size-sorting associated with the MY2 scheme when $\alpha = 0$, as discussed by MY05a. To confirm this, we repeated experiment 500mMY2 in which the size-sorting mechanism was effectively turned off by setting the fall speed for N_t equal to that of q for all categories; in this case, a smaller forward-flank region with a weaker reflectivity gradient was obtained (not shown).

The results of the 250-m experiments were qualitatively similar to those at 500-m grid spacing in regards to cold pool and reflectivity structure, suggesting that further refinement of the horizontal grid spacing beyond 500 m brings out little additional *qualitative* difference in storm structure and behavior, at least inasmuch as the impact of the BMP on reflectivity and cold pool structure are concerned. For this reason and the sake of brevity, we will focus on the 500-m simulations in the rest of this paper.

b. Budget analysis

A greater understanding of the differences in the roles of the various microphysical processes within the low-level downdraft in the different simulations can be obtained by performing detailed budget analyses of the microphysical source terms related to temperature change. At any point, the time rate of change of temperature due to phase changes of water can be written as

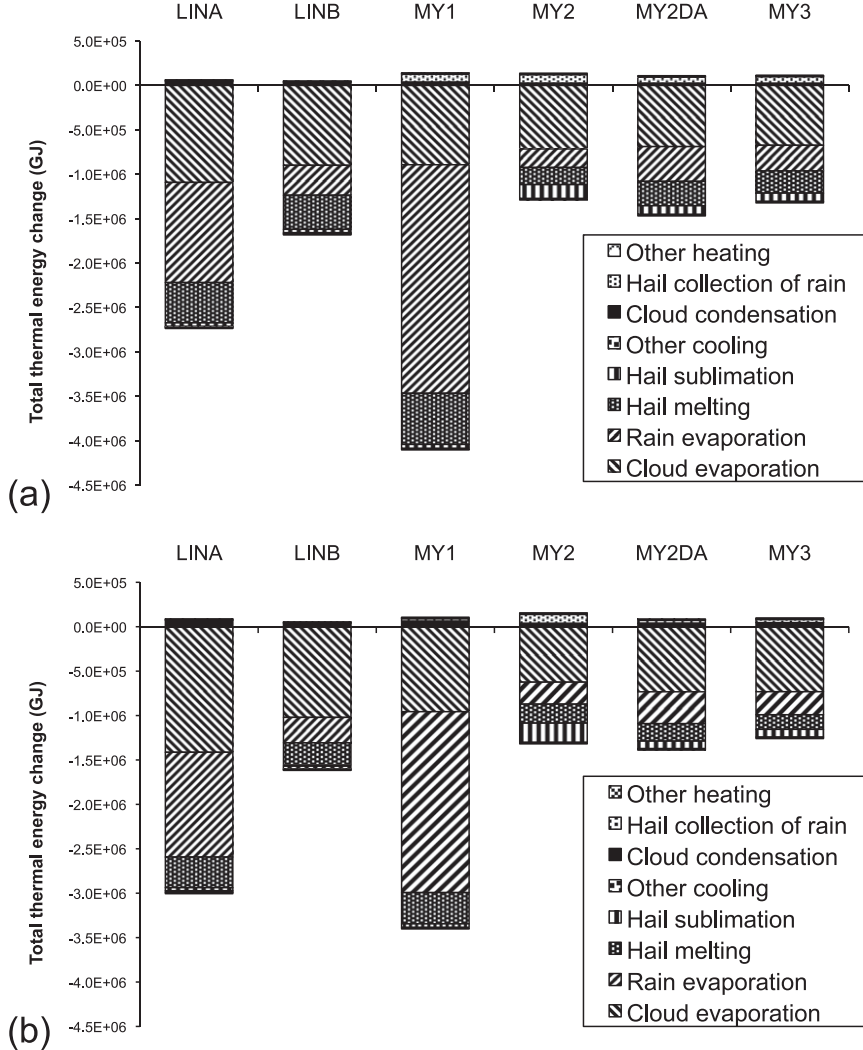


FIG. 8. Bulk thermal energy change ($c_p\Delta T$) from microphysical processes in the low-level downdraft (defined as all grid boxes below 4 km AGL with $w < -0.5 \text{ m s}^{-1}$) between (a) 1800 and 3600 s and (b) 3600 and 5400 s for each of the 500-m simulations.

$$\left. \frac{\partial T}{\partial t} \right|_{\text{mp}} = S_{\text{mp}}, \quad (4)$$

where the subscript mp denotes microphysical phase changes, and S_{mp} includes all source and sink terms involving phase changes of water. The processes include evaporation and condensation of cloud water; evaporation of rain; melting and freezing of ice crystals, snow, graupel, and hail; and collection (freezing) of cloud and rain by each of the above ice categories. Most of the processes are common to the schemes examined in this study. However, since the LIN scheme does not contain a separate graupel category, the associated processes are not active. In addition, neither the LIN nor MY scheme allows for condensation of vapor onto rain.

To determine the most important processes and how they differ among the simulations, the instantaneous rates of these processes were output at 30-s intervals for each of the simulations for two 30-min intervals: 1800–3600 and 3600–5400 s. Total cooling/heating is calculated for each of the processes by integrating (4) within each grid cell that is below 4 km AGL and has vertical velocity less than -0.5 m s^{-1} (defined as the downdraft region) and over each of the 30-min periods using a 30-s time step (that of the data interval), that is, $\Delta E_{\text{mp}} = \sum_{i,j,k,t} (\rho c_p \Delta T_{\text{mp}} \Delta x \Delta y \Delta z)$, where ρ is the air density, and Δx , Δy , and Δz are the local grid spacings in the x , y , and z directions, respectively. Furthermore, $\Delta T_{\text{mp}} = (L_{v,f,s}/c_p)\Delta q$, where $L_{v,f,s}$ is the appropriate latent heat of vaporization, fusion, or sublimation, respectively, and

Δq is the hydrometeor mixing ratio change due to the given process in the given grid cell.

The bulk heating/cooling budgets for the processes are shown in Fig. 8 for the 500-m simulations, in units of gigajoules (GJ). We emphasize that the budget calculations are restricted to regions below 4 km AGL, which is near the freezing level of the environment. Thus, processes which contribute to latent heating due to freezing are not significant, except for the case of rain freezing onto hailstones (which is typically compensated for later by melting at a lower level). The budgets indicate that, in general, evaporation of cloud, evaporation of rain, and melting of hail are the three most important processes contributing to cooling in the low-level downdrafts (hail sublimation is relatively more significant in the case of the MM runs). This is consistent with a previous numerical modeling study of microburst-producing storms by Straka and Anderson (1993). In general, the MM simulations are very similar in magnitude of total cooling, while the SM simulations differ from each other and from the MM simulations, particularly in regards to evaporation of rain. Of all the runs, 500mMY1 has by far the greatest magnitude of cooling, mainly due to more evaporation of rain. Even though the same intercept parameters were used in 500mMY1 and 500mLINA for all precipitating species, other differences in the schemes, such as in the treatment of the cloud category and the fall speed relation for the rain category are possible reasons for the differences in total cooling.

c. Spatiotemporal structure of rain evaporation and effects of DSD variation

Figure 9 shows a time series plot of the maximum instantaneous rain evaporation rate experienced below 4 km AGL within the low-level downdraft for each experiment for the 2-h simulation period. For most of the simulation period, consistent with the budget analysis, 500mMY1 has the largest maximum evaporation rates, followed by 500mLINA. The rapid drop in evaporation for 500mMY1 near 5400 s is due to the dissipation of the storm in this simulation around this time (cf. Fig. 4). The MM runs are similar to each other and 500mLINB in the overall trend of maximum evaporation rates, but notably, there appears to be a systematic increase in maximum evaporation for most of the simulation period when moving from MY2 to MY3 to MY2DA. To explain the differences in evaporative cooling between the simulations, we turn to an examination of the rain DSD parameters.

Vertical profiles of horizontally and time-averaged values (using the same criteria as in the budget analysis for the downdraft region) of mixing ratio, number con-

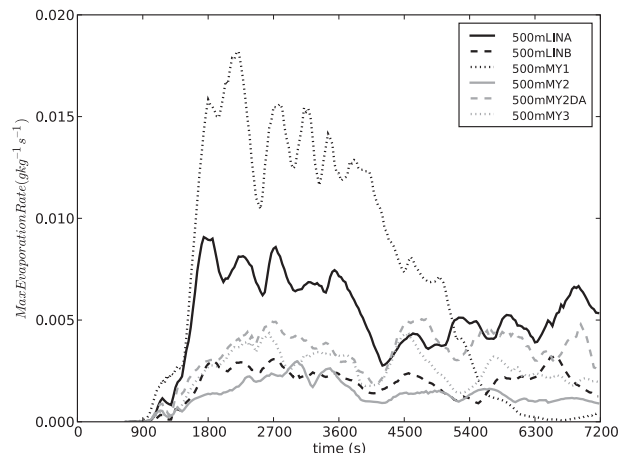


FIG. 9. Time series of maximum low-level (<4 km AGL) instantaneous evaporation rate ($\text{g kg}^{-1} \text{ s}^{-1}$) for each of the 500-m runs.

centration, mean-mass diameter, and shape parameter for rain (Fig. 10) were computed for the 500-m runs. Only grid points with nonzero hydrometeor content were included in the averaging. These plots suggest that two main differences between the MM and SM runs contribute to the smaller magnitudes of cooling in the low-level downdrafts in the MM cases: 1) the generally smaller mass contents of rain in the downdraft, and 2) the overall larger diameters of the drops in the MM runs, which limit the evaporation potential (due to the smaller surface area to volume ratio). Indeed, average number concentrations of rain are 1–3 orders of magnitude smaller in the MM runs than in the SM runs, while the mixing ratios are only a factor of 2 or less lower. This is reflected in the D_m profiles, which indicate significantly larger average drop diameters in the MM over most of the depth of the low-level downdraft. Figure 11 shows corresponding averaged profiles of rain intercept parameter and instantaneous evaporation rate. For 500mMY2DA and 500mMY3, the intercept parameter was first normalized using the method of Testud et al. (2001). The MM runs all show smaller N_0 over most of the depth of the low-level downdraft than any of the SM runs (Fig. 11a). To determine whether the variation in the DSD or the overall lower rain mass content in the downdraft was primarily responsible for the differences in evaporation between the SM and MM runs, hypothetical evaporation rates were calculated for each of the MM runs, using the same q , but assuming that the DSD at every point was actually exponential with $N_0 = 8.0 \times 10^6 \text{ m}^{-4}$ (i.e., as in 500mLINA and 500mMY1). These were then averaged in the same manner as the actual evaporation rates and plotted in Fig. 11b. Even with the smaller q , changing the form of the DSD in this

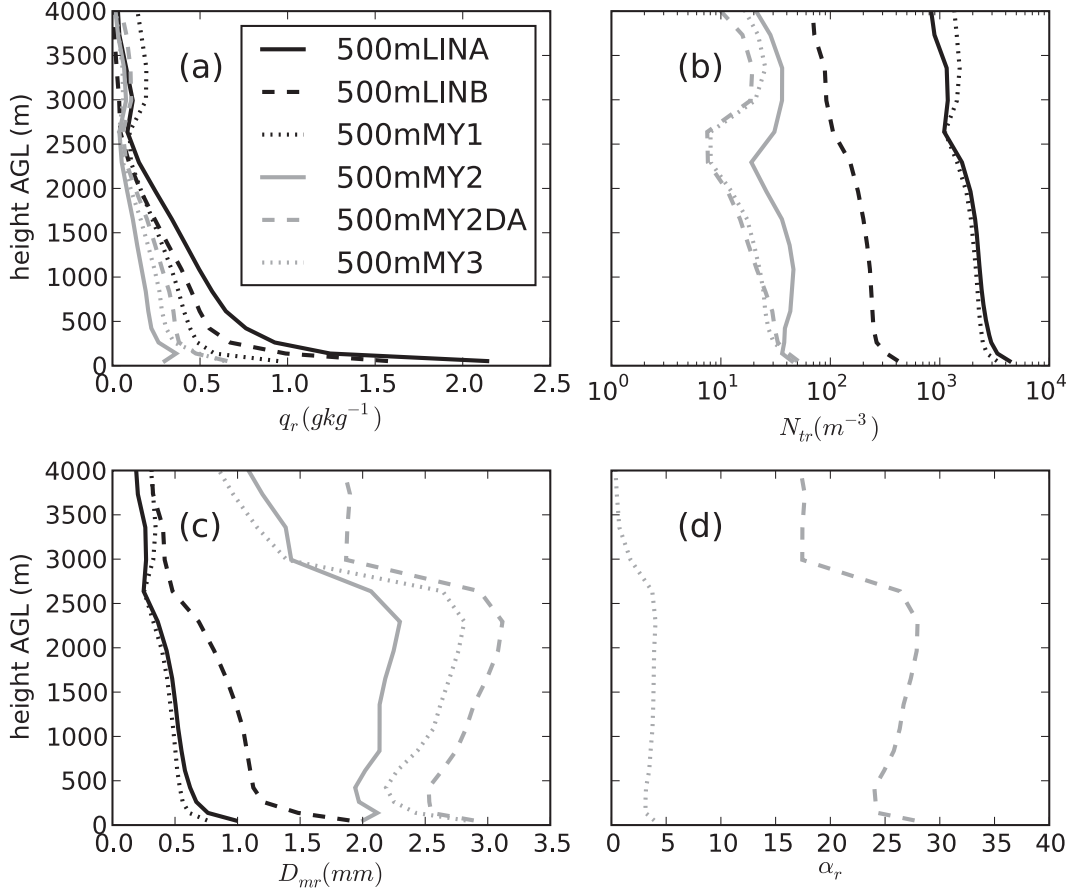


FIG. 10. Vertical profiles of horizontally and time-averaged rain DSD parameters in the low-level downdrafts of the 500-m simulations: (a) mixing ratio q_r , (b) total number concentration N_{tr} , (c) mean-mass diameter D_{mr} , and (d) shape parameter α_r .

manner clearly results in much greater evaporation rates than the actual situation, with, for example, 500mMY3 having a nearly identical profile as 500mMY1 using the MY1-DSD.

Recall that N_0 must be specified a priori in the SM runs. The difference in rain evaporative cooling between 500mLINA and 500mLINB is significant and directly attributable to the smaller fixed N_0 value used, which has a first-order effect on decreasing the rain evaporation rate. The bulk evaporation rate of rain [see MY05b, their Eq. (7)] can be written as

$$QVD_{vr} = \frac{2\pi(S_w - 1)N_{0r} VENT_r}{AB_w}, \quad (5)$$

where QVD_{vr} is the instantaneous change in rain mixing ratio due to evaporation, S_w is the saturation ratio with respect to water, $VENT_r$ is the bulk ventilation coefficient, and AB_w is the thermodynamic function (for further explanation of these terms, see MY05b).

Noteworthy is the fact that the bulk rain evaporation rate is proportional to the intercept parameter N_0 . All other things being equal, a reduction in N_0 will result in a corresponding reduction in evaporation rate. This is because changing N_0 while holding q constant preferentially affects the small drop end of the spectrum, where most of the evaporation takes place. The ventilation term, however, helps to counteract this tendency somewhat by accounting for enhanced evaporation of larger drops due to better ventilation. However, as pointed out by Cohen and McCaul (2006), these drops also fall faster and thus have less residence time in the air, which is parameterized in most bulk schemes by a larger mass-weighted terminal fall speed for the drop population.

The dependence of evaporation rate on N_0 explains the strong sensitivity to cold pool intensity and size seen in previous studies with SM schemes that varied the value of N_0 for rain and/or hail. However, observational studies and previous numerical simulations with DM BMPs have shown that N_0 can vary in time and space,

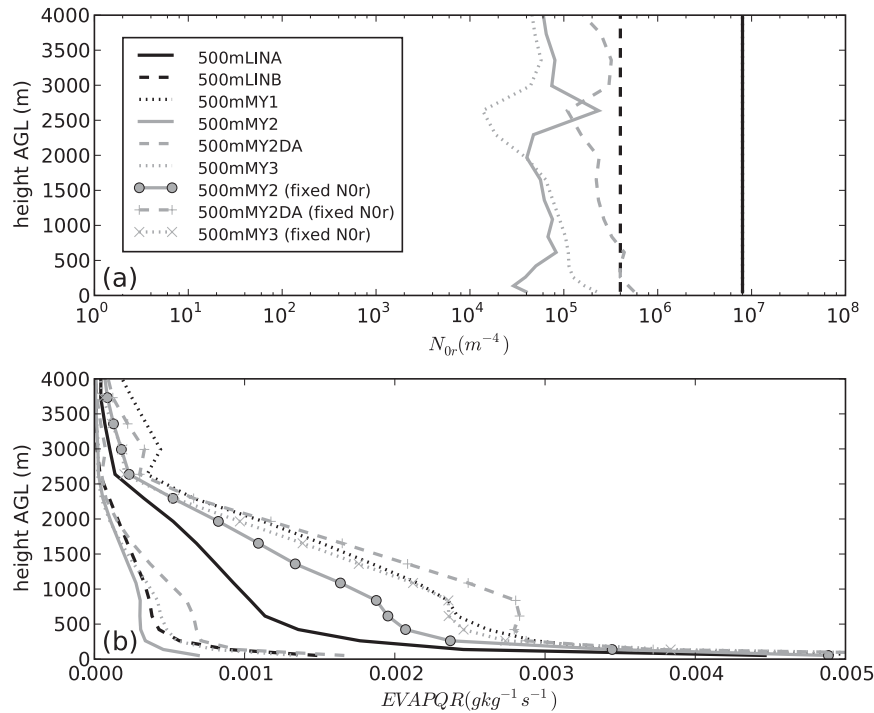


FIG. 11. As in Fig. 10 but for (a) (normalized) rain intercept parameter N_{0r} and (b) instantaneous evaporation rate. Also plotted in (b) are three curves corresponding to the hypothetical evaporation rates assuming exponential distributions and the MY1 fixed value of $N_{0r} = 8.0 \times 10^6 \text{ m}^{-4}$ for each of the runs 500mMY2, 500mMY2DA, and 500mMY3 (circle, plus, and \times markers, respectively).

even within the same convective system. An example is the change in N_0 between the convective and stratiform regions of a squall line: the so-called N_0 jump (Walvgogel 1974; Ferrier et al. 1995; Morrison et al. 2009). Thus, a fixed global value of N_0 may lead to large errors, even over the course of a simulation or prediction of the same case. As previously discussed, a MM scheme allows N_0 to vary independently and presumably consistently with the dynamical and microphysical processes. For a given precipitation event, N_0 may be on average larger, smaller, vary greatly, or vary slightly. This inherent flexibility is a primary reason MM schemes are attractive, because they effectively remove some of the difficulty in choosing the “correct” parameters in a SM scheme for a given situation.

Note that for 500mMY2DA and 500mMY3, the physical meaning of N_0 changes (see, e.g., Ulbrich 1983; Testud et al. 2001), due to the dependence on α , which is allowed to vary over a wide range of positive values [but note that the SM runs and 500mMY2 all assumed exponential distributions (i.e., $\alpha = 0$) for all precipitating hydrometeors]. It can be shown that an increase in α (i.e., narrowing the distribution) given q and N_t actually enhances evaporation because of an increase in the total surface area of the drops (Cohen and McCaul 2006).

This increase in evaporation rate by allowing the shape parameter to take on variable, positive values in 500mMY2DA and 500mMY3 is consistent with the overall larger evaporation rates in these runs as opposed to 500mMY2 (cf. Fig. 9).

It is also instructive to examine the spatial structure of rain evaporation at a given time across the simulations. Figure 12 shows the rainwater-mixing ratio q_r , instantaneous evaporation rate, and negative vertical velocity w contours (downdrafts) at 500 m AGL and 1 h of the 500-m simulations. Figure 13 shows the same fields but through the vertical cross sections indicated in Fig. 12. It can be seen that significant differences exist between the spatial structure of instantaneous rates associated with different BMPs, and in particular between those of the SM and MM schemes. The SM schemes show larger magnitudes and greater vertical depths of evaporation, and overall stronger downdrafts as compared to the DM or TM schemes, except that 500mLINB shows the smallest rain evaporation rates. In addition, the SM schemes tend to produce pronounced FFDs that reach the surface, whereas the MM schemes feature *elevated* FFDs, that is, FFDs that do not reach the ground. Romine et al. (2008) found similar results in their study of the 8 May 2003 Moore, Oklahoma, supercell, and attributed

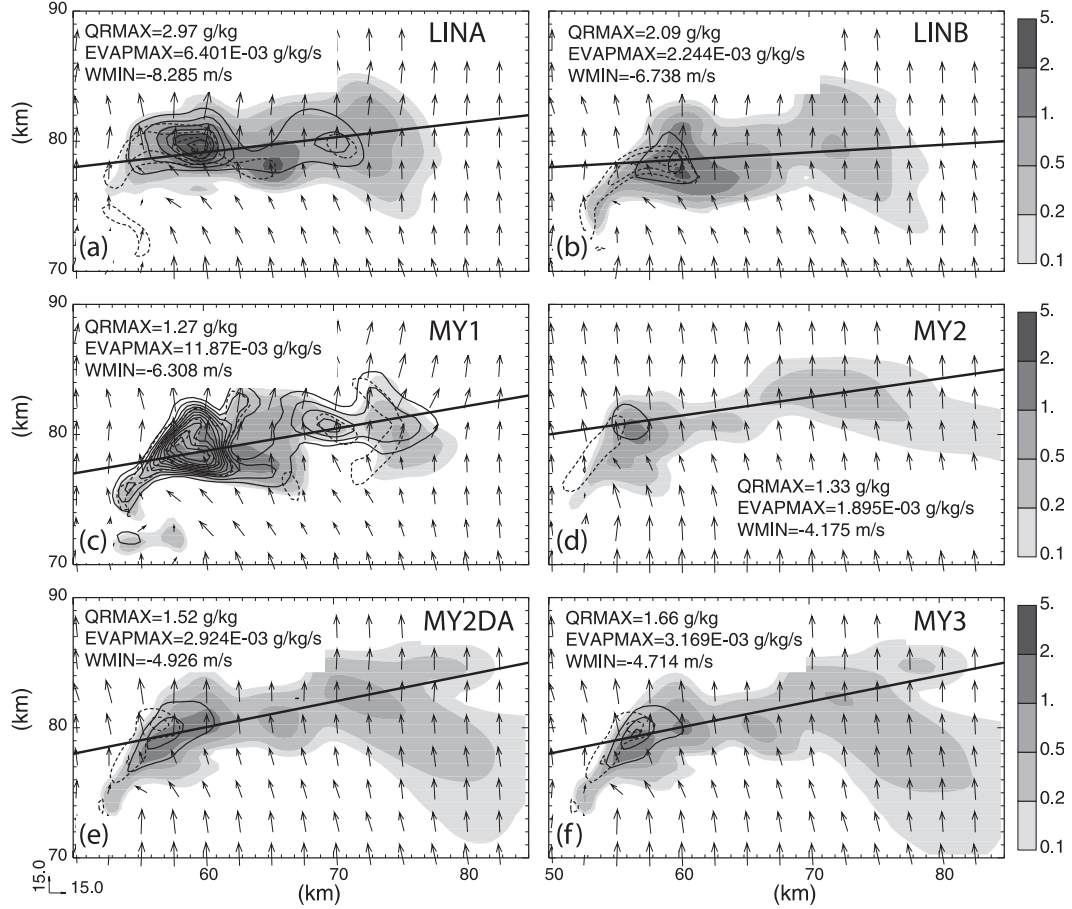


FIG. 12. Rain mixing ratio (grayscale filled contours, g kg^{-1}), instantaneous evaporation rate (black contours, $1.0 \times 10^{-3} \text{ g kg}^{-1} \text{ s}^{-1}$ increment), negative vertical velocity (dashed contours, 2 m s^{-1} increment, starting at -2 m s^{-1}) and wind vectors at 500 m AGL at 1 h for (a) 500mLINA, (b) 500mLINB, (c) 500mMY1, (d) 500mMY2, (e) 500mMY2DA, and (f) 500mMY3. Maximum values of q_r and rain evaporation rate and minimum values of vertical velocity are indicated. Also shown are the locations of the vertical cross sections shown in Fig. 13.

it at least partially to the relatively weak FFD being unable to penetrate the capping inversion present in the environment of the storm. In the present study, however, no capping inversion is present, and thus it appears that the differences in this case are mainly related to the different BMPs used. Instantaneous fields at other times indicate similar structure (not shown).

d. Cold bias in SM evaporation as revealed through comparison with MM

While an exhaustive study of all possible microphysical processes parameterized in the bulk schemes herein and especially their different treatments between the SM and MM approach, would be the most rigorous approach to explaining the resulting effects on the DSDs in the low-level downdrafts, the sheer complexity of the problem and the myriad nonlinear interactions that must be considered are significant. Nevertheless, we

have identified two microphysical processes that significantly affect the DSD in the subsaturated low-level downdrafts that together appear to explain many of the differences between SM and MM in this region of convective storms, and also lead to a cold bias in SM, independent of the choice of N_0 . These are the evaporation process itself, and the size-sorting mechanism. We stress that other processes operating concurrently or “upstream” in the storm in time and space are not considered in detail here, but may also be important, especially the initial cloud droplet spectrum, growth rates of rain and hail, and the interaction of the rain and hail fields both prior to the populations entering the low-level downdraft, and within the low-level downdraft itself.

We have already seen that MM BMPs allow for a size-sorting mechanism, while SM BMPs do not. MY05a found that size sorting is one reason for the larger values

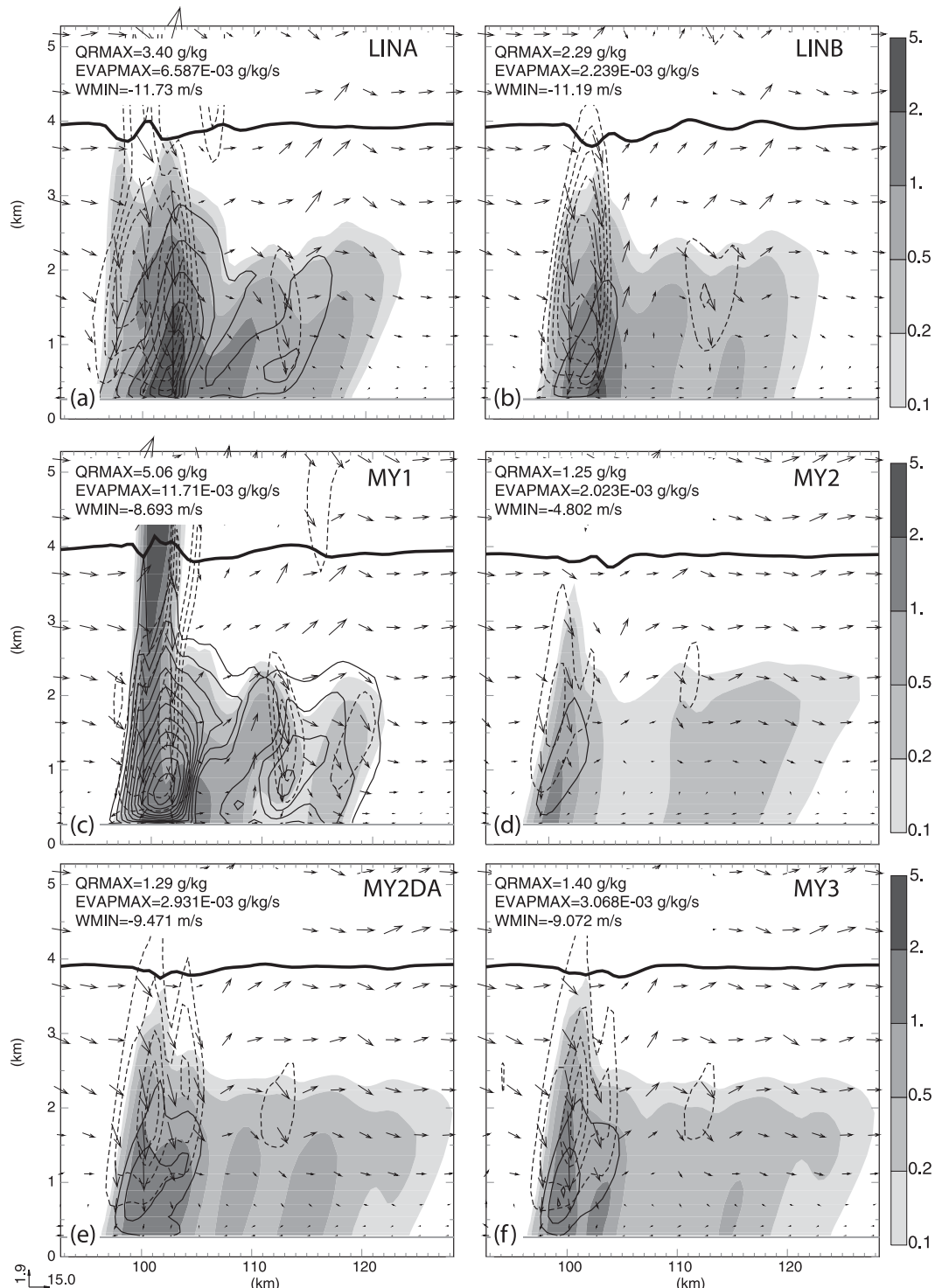


FIG. 13. As in Fig. 12, but for the vertical cross sections depicted in Fig. 12. The 0°C isotherm is also shown in thick black lines.

of D_m (and thus smaller N_0 in the exponential MY2 case) at the low levels, as compared to the SM case. The rain distribution under the influence of size sorting becomes skewed toward larger drop diameters in the lower levels, leading to smaller magnitudes of evaporation in the low-level downdrafts. In a SM scheme, however, because a single (typically mass weighted) fall speed is used, this effectively leads to the unphysical behavior of the smallest particles falling too quickly, and the largest particles too slowly. This directly translates into larger, unphysical, evaporation rates in the low levels (cf. Figs. 11b and Fig. 13). It is worth emphasizing at this point that size sorting cannot even be modeled without allowing independent variation of the distribution parameters (e.g., one cannot fix N_0 and still model size sorting).

For a SM scheme that fixes N_0 , evaporation of a population of raindrops necessarily yields an increase in slope. This leads to yet another unphysical behavioral characteristic of SM schemes that fix N_0 . An increase in slope λ for an exponential distribution, while reducing q and holding N_0 constant, is physically equivalent to reducing the concentration of the largest drops from the distribution faster than the concentration of the drops at the small drop end of the spectrum, a result contradicting physical intuition and the results of theoretical studies on evaporation within rain shafts (e.g., Tzivion et al. 1989; Li and Srivastava 2001). It can be seen that evaporation in the fixed- N_0 case actually shifts the entire drop population toward smaller diameters, leaving a considerable number of small-to-medium-sized drops contributing to high evaporation rates; in reality these drops are likely to be quickly depleted (except for perhaps the very smallest drops; see previous references). We believe that these two unphysical effects, together with a choice of fixed N_0 that is too large, are significant factors contributing to the large evaporation rates and the attendant strong downdrafts and cold pools seen in many past and contemporary simulations of convective storms using typical SM schemes. However, SM schemes that specify the mean-mass diameter D_m or characteristic diameter D_n (e.g., van den Heever and Cotton 2004) instead of N_0 would not suffer from the particular issue of the increase of slope during evaporation (since choosing a fixed characteristic diameter is equivalent to fixing the slope), while the issue of sensitivity to the choice of parameter values still remains. On the other hand, in the MM schemes used in this study, the slope (and thus D_m) is assumed to remain constant during the process of evaporation. As such, evaporation would reduce both q and N_t at the same relative rate, leading to a corresponding reduction in N_0 for the exponential DSD case. Physically, this translates to individual par-

ticles across the distribution being shifted down the spectrum toward smaller sizes as they evaporate, with the population as a whole maintaining the same mean mass. The smallest drops leave the distribution at the small end by being converted to vapor, a process much more physically reasonable than the SM case. This DM closure assumption for the rate of decrease in N_t is still not entirely correct, however, since it implies that the mean-mass drop diameter does not change because of evaporation, and thus overestimates the rate of decrease in N_t (Seifert 2008). Nevertheless, it is a distinct improvement over the fixed- N_0 assumption used in most SM schemes.

e. 1D column model tests

To test the above hypotheses regarding the effects of size sorting and the differences between the treatments of pure evaporation in the SM and MM cases, we performed idealized 1D simulations of a distribution of raindrops falling in subsaturated air, using all four versions of the MY scheme. To cleanly isolate these effects, the simulations were made as simple as possible, while still being physically reasonable. The following restrictions were applied: only the processes of rain evaporation and sedimentation were modeled and no collision or breakup were allowed [the reader is referred to Feingold et al. (1991) for a discussion on the importance of these effects on evaporation]. The atmosphere was assumed quiescent and isentropic with a base-state potential temperature of 300 K, a surface pressure of 1000 hPa, and a constant saturation ratio of 0.6. No feedback from the evaporation of the falling rain to the atmosphere was allowed to either the temperature or moisture fields. At the top boundary, rainwater with an exponential distribution and a q_r of 1 g kg^{-1} was specified as the boundary condition for the falling rain field, with a constant intercept parameter of $8.0 \times 10^6 \text{ m}^{-4}$ (i.e., that of the well-known Marshall–Palmer distribution; Marshall and Palmer 1948). The initial q_r was zero inside the domain. The vertical grid spacing was a uniform 100 m over a depth of 5 km, and a time step of 5 s was used.

The results of the tests are summarized in Fig. 14. In addition to the four control simulations shown in Figs. 14a–d where both size sorting and evaporation are active, results using the MY2, MY2DA, and MY3 schemes but with size sorting turned off are also shown (Figs. 14e–g). The vertical profiles all reached a steady state after approximately 30–45 min and thus those at 45 min are shown. As expected, the MY1 scheme shows the most evaporation over the greatest depth, followed by the MY3, MY2DA, and MY2 schemes in order of decreasing evaporation. The removal of size sorting leads

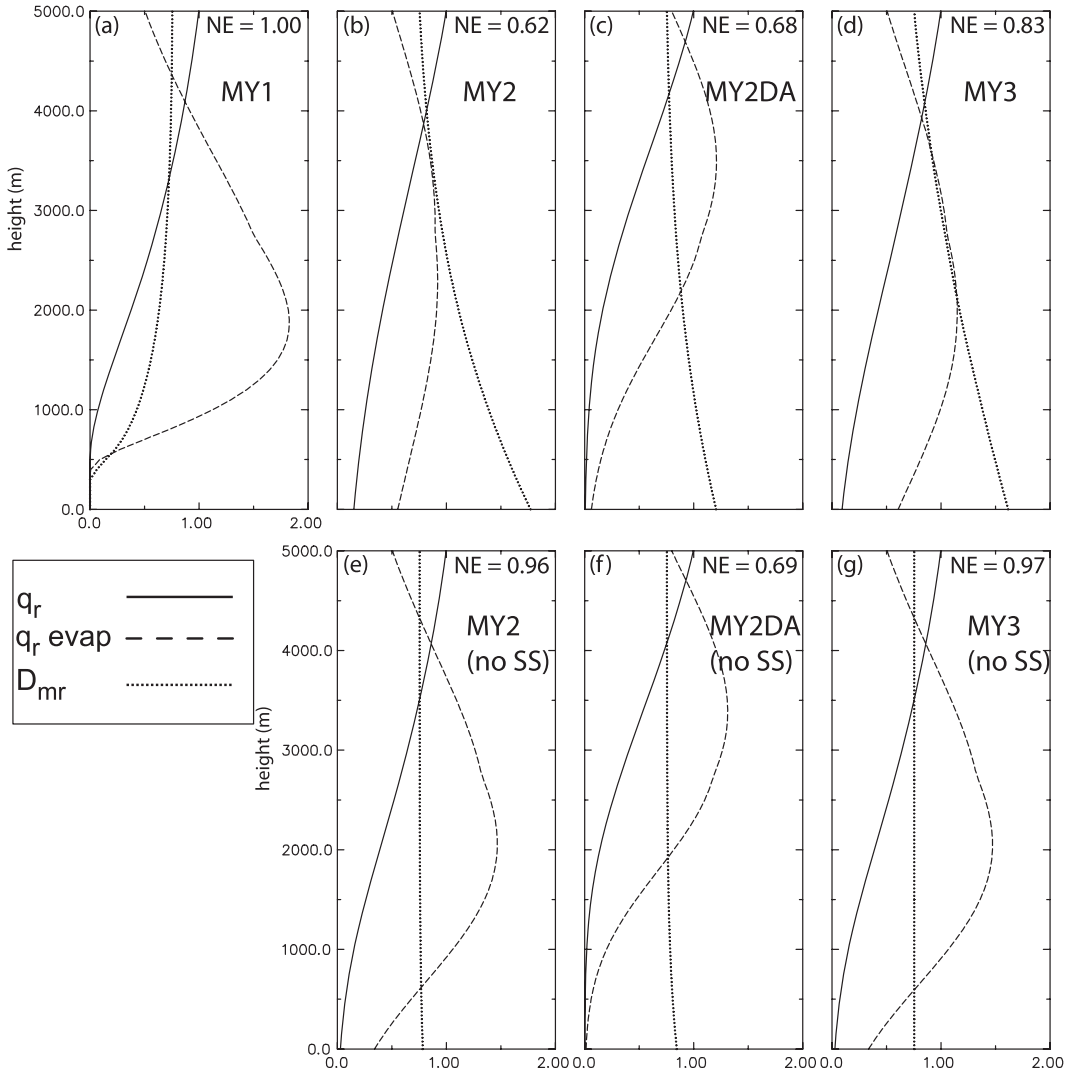


FIG. 14. Vertical profiles of rain mixing ratio q_r (kg kg^{-1} , solid), mean-mass diameter D_{mr} (m, dotted), and evaporation rate ($\text{kg kg}^{-1}\text{s}^{-1} \times 1000$, dashed) for the simple sedimentation–evaporation column model for (a) MY1, (b) MY2, (c) MY2DA, (d) MY3, (e) MY2 with no size sorting, (f) MY2DA with no size sorting, and (g) MY3 with no size sorting. Also shown is the normalized total evaporation (NE) over the previous 45 min relative to the MY1 scheme.

to stronger and deeper evaporation, though not as great as the MY1 case.

The results of the 1D column experiments corroborate the argument that size sorting on one hand, and the improved treatment of evaporation on the other, in the MM schemes, both lead to reduced evaporation of a falling rain shaft, and by extension, weaker, shallower downdrafts and weaker cold pools, relative to the SM schemes. Again, in the case of size sorting, the SM schemes cannot model this process, and, in the case of evaporation, the MM schemes are free to specify a different relationship between N_0 and λ relative to other processes (in this case, by fixing λ instead of N_0). How-

ever, the results of the 1D column experiments also indicate that the effect of size sorting on the independent variation of N_0 and λ appears to be of primary importance relative to that due to the processes of evaporation and melting (cf. top and bottom rows of Fig. 14). In contrast, tests with the full 3D model, where size sorting was turned off in the MY2 scheme (not shown) suggest that, in the full 3D framework where more processes are active, the overall impact of size sorting is less than might be expected given the 1D tests, although still discernable. Our ongoing research is continuing to examine the relative importance of these various processes in MM schemes.

5. Conclusions

In this paper, we have performed high-resolution idealized simulations of the 3 May 1999 Oklahoma tornadic supercell thunderstorms. The goal of this study was to test the impact of a new multimoment (MM) microphysics scheme on the evolution of the storms, and in particular on the rain DSD and its impact on the downdraft and cold pool properties. We found that the MM schemes, in general, performed better than their single-moment (SM) counterparts employing typical values of the intercept parameters. At the relatively coarse horizontal grid spacing of 3 km in the real-data simulations, all schemes produced cold pools that were too cold and dry, relative surface mesonet observations (see Dawson et al. 2007). However, in the idealized simulations at horizontal grid spacings of 500 and 250 m, the MM schemes showed clear and significant improvements in the cold pool and reflectivity structures of the storms compared to the observations. The MM schemes showed overall weaker and moister cold pools, which is consistent with available observations. In addition, the forward-flank region was more developed and closer to the size and shape of the observed forward-flank regions of the mature supercells on this day. This was attributed at least partially to the process of size sorting of hydrometeors, which is reasonably handled in the MM schemes, but not in the SM schemes (MY05a).

We further demonstrated through a budget analysis that the MM schemes yield less water mass in the low-level downdrafts and larger average drop sizes, both of which lead to significantly lower amounts of evaporation and associated diabatic cooling. The vertical profiles of evaporation are also altered in the MM schemes, with significantly less evaporation near the surface, particularly in the forward-flank region of the storm. Thus, while the forward-flank downdraft reaches the surface at times in the SM simulations, it remains elevated above the surface in the MM simulations, which is more consistent with the observations. In addition, the source region of the air reaching the surface in the downdrafts is significantly lower in the troposphere in the MM simulations than in the SM ones, as is also reflected by the higher θ_e in the cold pools of the MM storms.

Through an examination of the parameterized processes of evaporation and size sorting in the BMPs used in this study, we show that the MM schemes have a few important advantages over the SM schemes in their treatment of these processes, which are mostly related to how the drop size distributions (DSDs) are allowed to evolve in the MM schemes. In particular, a proper treatment of size sorting of rain leads to a distribution

skewed toward more large drops at the low levels, and hence less evaporation there. Also, the change in the DSD during evaporation is handled in a more physically realistic manner in the MM schemes by allowing N_0 to decrease during the evaporation process, while SM schemes hold it fixed. Results from a simplified column model highlighting sedimentation and evaporation confirm the role of the above processes. Taken together, the above two advantages with the MM schemes, and likely other direct and indirect effects, lead to a much better representation of evaporation in the low-level downdrafts of the simulated supercell storms examined in this study.

We note that while we have focused on the rain category in this paper, the physical arguments made herein also apply to other hydrometeor categories, especially hail and the process of hail melting, and in fact the MM runs also indicate less melting of hail than the SM runs in these simulations. In addition, we point out that while one can “tweak” a SM scheme to produce results similar to the MM schemes, this requires a priori knowledge of the type of storm and environment in the study and neglects the spatiotemporal variation of N_0 . Even so, the results of this study show that relevant physical parameterizations are handled poorly in SM versus MM. The added flexibility of MM schemes and their improved physical consistency over SM are strong arguments for their future increased use in convective storm modeling. Since low-level evaporation and resultant differences in cold pool strength and size have been shown in numerous studies to have a profound effect on the evolution of convective storms, even to the point of changing the mode of convection (from, e.g., discrete supercells to a more linear mode of convection; see, e.g., Snook and Xue 2008), the importance of accurate simulation of these processes cannot be overstated. Finally, we note that MM schemes are more computationally expensive than SM, with an approximately 75% increase in total computing time required between 500mLINA and 500mMY3 in this study, but the continued rapid increase in computing resources continues to make this argument against using MM microphysics less forceful.

As ongoing work, we are revisiting the real-data simulations with the smaller grid spacings used in the idealized simulations to examine the robustness of the idealized results under more realistic settings. The storm environment in this follow-up study is inhomogeneous and complete physical processes are included. We have also begun to extend the simulations to even higher resolutions to examine the impact of the BMP on tornadogenesis. Preliminary results are encouraging and indicate that the MM schemes produce much more realistic storm evolution and tornadic behavior when compared with the actual storm, with one of the MM runs

producing a tornado track that is very similar to the observed F5 tornado track. This can be considered the MM extension of the SM study by Snook and Xue (2008), which examined the microphysical effects on tornadogenesis. In addition, we plan to examine other MM schemes, such as the DM scheme of Morrison et al. (2005). Preliminary tests of the Morrison scheme as compared to the MY scheme suggest that differences between these schemes, especially in the treatment of the initial CCN activation and in the cloud autoconversion to rain may be just as large as the differences between the SM and MM schemes examined in this study, indicating that a more rigorous examination of the treatment of the relevant processes in these schemes is necessary. Finally, we wish to make a more rigorous comparison of the results of the MM simulations of the hydrometeor fields in the supercells with observations, such as by comparing them with polarimetric radar retrievals of hydrometeor fields.

Acknowledgments. This work was primarily supported by NSF Grants ATM-0530814 and ATM-0802888, the National Defense Science and Engineering Graduate Research Fellowship, and the National Science Foundation Graduate Fellowship, both awarded to the first author. Most of the computing for this study was performed at the OU Supercomputing Center for Education and Research (OSCER) at the University of Oklahoma (OU). Additional computing was performed on the Pittsburgh Supercomputing Center (PSC) machine *bigben*, and the Texas Advanced Computing Center (TACC) machine *ranger*, both TeraGrid resources. The authors thank Dr. Yunheng Wang for his initial implementation of the MY scheme into the ARPS model, Drs. Lou Wicker, Ted Mansell, Chuck Doswell, and Hugh Morrison for helpful discussions and suggestions, and two anonymous reviewers who contributed to the substantial improvement of the manuscript.

REFERENCES

- Bolton, D., 1980: The computation of equivalent potential temperature. *Mon. Wea. Rev.*, **108**, 1046–1053.
- Bryan, G. H., J. C. Wyngaard, and J. M. Fritsch, 2003: Resolution requirements for the simulation of deep moist convection. *Mon. Wea. Rev.*, **131**, 2394–2416.
- Cohen, C., and E. W. McCaul, 2006: The sensitivity of simulated convective storms to variations in prescribed single-moment microphysics parameters that describe particle distributions, sizes, and numbers. *Mon. Wea. Rev.*, **134**, 2547–2565.
- Dawson, D. T., II, M. Xue, J. A. Milbrandt, M. K. Yau, and G. Zhang, 2007: Impact of multi-moment microphysics and model resolution on predicted cold pool and reflectivity intensity and structures in the Oklahoma tornadic supercell storms of 3 May 1999. Preprints, 22nd Conf. on Weather Analysis and Forecasting/18th Conf. on Numerical Weather Prediction, Salt Lake City, UT, Amer. Meteor. Soc., 10B.2.
- Doswell, C. A., III, and D. W. Burgess, 1993: Tornadoes and tornadic storms: A review of conceptual models. *The Tornado: Its Structure, Dynamics, Prediction, and Hazards*, Geophys. Monogr., Vol. 79, Amer. Geophys. Union, 75–88.
- Feingold, G., Z. Levin, and S. Tzivivon, 1991: The evolution of raindrop spectra. Part III: Downdraft generation in an axisymmetrical rainshaft model. *J. Atmos. Sci.*, **48**, 315–330.
- Ferrier, B. S., 1994: A double-moment multiple-phase four-class bulk ice scheme. Part I: Description. *J. Atmos. Sci.*, **51**, 249–280.
- , W.-K. Tao, and J. Simpson, 1995: A double-moment multiple-phase four-class bulk ice scheme. Part II: Simulations of convective storms in different large-scale environments and comparisons with other bulk parameterizations. *J. Atmos. Sci.*, **52**, 1001–1033.
- Gilmore, M. S., and L. J. Wicker, 1998: The influence of mid-tropospheric dryness on supercell morphology and evolution. *Mon. Wea. Rev.*, **126**, 943–958.
- , J. M. Straka, and E. N. Rasmussen, 2004: Precipitation uncertainty due to variations in precipitation particle parameters within a simple microphysics scheme. *Mon. Wea. Rev.*, **132**, 2610–2627.
- Gunn, K. L. S., and J. S. Marshall, 1958: The distribution with size of aggregate snow flakes. *J. Meteor.*, **15**, 452–461.
- James, R. P., and P. M. Markowski, 2010: A numerical investigation of the effects of dry air aloft on deep convection. *Mon. Wea. Rev.*, **138**, 140–161.
- Lemon, L. R., and C. A. Doswell, 1979: Severe thunderstorm evolution and mesocyclone structure as related to tornadogenesis. *Mon. Wea. Rev.*, **107**, 1184–1197.
- Li, X., and R. C. Srivastava, 2001: An analytical solution for raindrop evaporation and its application to radar rainfall measurements. *J. Appl. Meteor.*, **40**, 1607–1616.
- Lin, Y.-L., R. D. Farley, and H. D. Orville, 1983: Bulk parameterization of the snow field in a cloud model. *J. Climate Appl. Meteor.*, **22**, 1065–1092.
- Mansell, E. R., 2008: EnKF analysis and forecast predictability of a tornadic supercell storm. Preprints, 24th Conf. on Severe Local Storms, Savannah, GA, Amer. Meteor. Soc., P5.2.
- Markowski, P. M., 2002: Mobile mesonet observations on 3 May 1999. *Wea. Forecasting*, **17**, 430–444.
- , J. M. Straka, and E. N. Rasmussen, 2002: Direct surface thermodynamic observations within the rear-flank downdrafts of nontornadic and tornadic supercells. *Mon. Wea. Rev.*, **130**, 1692–1721.
- Marshall, J. S., and W. M. Palmer, 1948: The distribution of raindrops with size. *J. Meteor.*, **5**, 165–166.
- McCaul, E. W., and C. Cohen, 2002: The impact on simulated storm structure and intensity of variations in the mixed layer and moist layer depths. *Mon. Wea. Rev.*, **130**, 1722–1748.
- Meyers, M. P., R. L. Walko, J. R. Harrington, and W. R. Cotton, 1997: New RAMS cloud microphysics parameterization. Part II: The two-moment scheme. *Atmos. Res.*, **45**, 3–39.
- Milbrandt, J. A., and M. K. Yau, 2005a: A multimoment bulk microphysics parameterization. Part I: Analysis of the role of the spectral shape parameter. *J. Atmos. Sci.*, **62**, 3051–3064.
- , and —, 2005b: A multimoment bulk microphysics parameterization. Part II: A proposed three-moment closure and scheme description. *J. Atmos. Sci.*, **62**, 3065–3081.
- , and —, 2006a: A multimoment bulk microphysics parameterization. Part III: Control simulation of a hailstorm. *J. Atmos. Sci.*, **63**, 3114–3136.

- , and —, 2006b: A multimoment bulk microphysics parameterization. Part IV: Sensitivity experiments. *J. Atmos. Sci.*, **63**, 3137–3159.
- Morrison, H., J. A. Curry, and V. I. Khvorostyanov, 2005: A new double-moment microphysics parameterization for application in cloud and climate models. Part I: Description. *J. Atmos. Sci.*, **62**, 1665–1677.
- , G. Thompson, and V. Tatarskii, 2009: Impact of cloud microphysics on the development of trailing stratiform precipitation in a simulated squall line: Comparison of one- and two-moment schemes. *Mon. Wea. Rev.*, **137**, 991–1007.
- Reisner, J., R. M. Rasmussen, and R. T. Bruntjes, 1998: Explicit forecasting of supercooled liquid water in winter storms using the MM5 mesoscale model. *Quart. J. Roy. Meteor. Soc.*, **124**, 1071–1107.
- Roeber, P. J., D. M. Schultz, and R. Romero, 2002: Synoptic regulation of the 3 May 1999 tornado outbreak. *Wea. Forecasting*, **17**, 399–429.
- Romine, G. S., D. C. Dowell, and R. B. Wilhelmson, 2008: Bridging the gap between observed and simulated supercell cold pool characteristics. Preprints, *24th Conf. on Severe Local Storms*, Savannah, GA, Amer. Meteor. Soc., 15.16.
- Saleeby, S. M., and W. R. Cotton, 2004: A large-droplet mode and prognostic number concentration of cloud droplets in the Colorado State University Regional Atmospheric Modeling System (RAMS). Part I: Module descriptions and supercell test simulations. *J. Appl. Meteor.*, **43**, 182–195.
- Seifert, A., 2008: On the parameterization of evaporation of raindrops as simulated by a one-dimensional rainshaft model. *J. Atmos. Sci.*, **65**, 3608–3619.
- , and K. D. Beheng, 2001: A double-moment parameterization for simulating autoconversion, accretion and self-collection. *Atmos. Res.*, **59–60**, 265–281.
- , and —, 2006: A two-moment cloud microphysics parameterization for mixed-phase clouds. Part 1: Model description. *Meteor. Atmos. Phys.*, **92**, 45–66.
- , A. Khain, A. Pokrovsky, and K. D. Beheng, 2006: A comparison of spectral bin and two-moment bulk mixed-phase cloud microphysics. *Atmos. Res.*, **80**, 46–66.
- Snook, N., and M. Xue, 2008: Effects of microphysical drop size distribution on tornadogenesis in supercell thunderstorms. *Geophys. Res. Lett.*, **35**, L24803, doi:10.21029/22008GL035866.
- Speheger, D. A., C. A. Doswell, and G. J. Stumpf, 2002: The tornadoes of 3 May 1999: Event verification in central Oklahoma and related issues. *Wea. Forecasting*, **17**, 362–381.
- Straka, J. M., and J. R. Anderson, 1993: Numerical simulations of microburst producing storms: Some results from storms observed during COHMEC. *J. Atmos. Sci.*, **50**, 1329–1348.
- , M. S. Gilmore, K. M. Kanak, and E. N. Rasmussen, 2005: A comparison of the conservation of number concentration for the continuous collection and vapor diffusion growth equations using one- and two-moment schemes. *J. Appl. Meteor.*, **44**, 1844–1849.
- Tao, W.-K., and J. Simpson, 1993: Goddard cumulus ensemble model. Part I: Model description. *Terr. Atmos. Ocean Sci.*, **4**, 35–72.
- Testud, J., S. Oury, R. A. Black, P. Amayenc, and X. Dou, 2001: The concept of “normalized” distribution to describe raindrop spectra: a tool for cloud physics and cloud remote sensing. *J. Appl. Meteor.*, **40**, 1118–1140.
- Thompson, R. L., and R. Edwards, 2000: An overview of environmental conditions and forecast implications of the 3 May 1999 tornado outbreak. *Wea. Forecasting*, **15**, 682–699.
- Tzivivon, S., G. Feingold, and Z. Levin, 1989: The evolution of raindrop spectra. Part II: Collisional collection/breakup and evaporation in a rainshaft. *J. Atmos. Sci.*, **46**, 3312–3328.
- Ulbrich, C. W., 1983: Natural variations in the analytical form of the raindrop size distribution. *J. Climate Appl. Meteor.*, **22**, 1204–1215.
- van den Heever, S. C., and W. R. Cotton, 2004: The impact of hail size on simulated supercell storms. *J. Atmos. Sci.*, **61**, 1596–1609.
- Waldvogel, A., 1974: The N_0 -jump of raindrop spectra. *J. Atmos. Sci.*, **31**, 1067–1078.
- Walko, R. L., W. R. Cotton, M. P. Meyers, and J. L. Harrington, 1995: New RAMS cloud microphysics parameterization. Part I: The single-moment scheme. *Atmos. Res.*, **38**, 29–62.
- Xue, M., 2000: High-order monotonic numerical diffusion and smoothing. *Mon. Wea. Rev.*, **128**, 2853–2864.
- , K. K. Droegemeier, and V. Wong, 2000: The Advanced Regional Prediction System (ARPS)—A multiscale nonhydrostatic atmospheric simulation and prediction tool. Part I: Model dynamics and verification. *Meteor. Atmos. Phys.*, **75**, 161–193.
- , D.-H. Wang, J.-D. Gao, K. Brewster, and K. K. Droegemeier, 2003: The Advanced Regional Prediction System (ARPS), storm-scale numerical weather prediction, and data assimilation. *Meteor. Atmos. Phys.*, **82**, 139–170.